

OPEN ACCESS

Ion Transport Mechanisms in the Oxide Film Formed on 316L Stainless Steel Surfaces Studied by ToF-SIMS with $^{18}\text{O}_2$ Isotopic Tracer

To cite this article: Luntao Wang *et al* 2020 *J. Electrochem. Soc.* **167** 101511

View the [article online](#) for updates and enhancements.

You may also like

- [The Effects of Perfluoroalkyl and Alkyl Backbone Chains, Spacers, and Anchor Groups on the Performance of Organic Compounds as Corrosion Inhibitors for Aluminum Investigated Using an Integrative Experimental-Modeling Approach](#)
I. Milošev, A. Kokalj, M. Poberžnik *et al.*
- [Electrochemical and Passive Layer Characterizations of 304L, 316L, and Duplex 2205 Stainless Steels in Thiosulfate Gold Leaching Solutions](#)
Maysam Mohammadi, Lokesh Choudhary, Ibrahim M. Gadala *et al.*
- [Roles of Chloride Ions in the Formation of Corrosion Protective Films on Copper](#)
Dževad K. Kozlica, Jernej Ekar, Janez Kova *et al.*



Your Lab in a Box!

The PAT-Tester-i-16: All you need for Battery Material Testing.

- ✓ All-in-One Solution with integrated Temperature Chamber!
- ✓ Cableless Connection for Battery Test Cells!
- ✓ Fully featured Multichannel Potentiostat / Galvanostat / EIS!

www.el-cell.com +49 40 79012-734 sales@el-cell.com

EL-CELL[®]
electrochemical test equipment





Ion Transport Mechanisms in the Oxide Film Formed on 316L Stainless Steel Surfaces Studied by ToF-SIMS with $^{18}\text{O}_2$ Isotopic Tracer

Luntao Wang, Antoine Seyeux, and Philippe Marcus^{*,z} 

Chimie ParisTech-CNRS, PSL University, IRCP, Physical Chemistry of Surfaces Group, 75005 Paris, France

The composition and structure of the native and passive oxide films formed on 316 L stainless steel have been studied in situ by ToF-SIMS. High temperature re-oxidation experiments in isotopic $^{18}\text{O}_2$ gas have also been done to assess the ion transport mechanisms in the native and passive oxide films. Duplex oxides with an inner Cr rich layer and an outer layer rich in Fe and Mo oxide have been observed on native and passive oxide films. Exposure of the oxide films to isotopic $^{18}\text{O}_2$ tracer at 300 °C reveals that the outward cationic diffusion governs the inner oxide growth. The outer Mo-rich layer prevents the continued transport of Cr to the outermost surface. The passive film, due to its composition and structure, exhibits a markedly lower oxidation rate compared to native oxide films.

© 2020 The Author(s). Published on behalf of The Electrochemical Society by IOP Publishing Limited. This is an open access article distributed under the terms of the Creative Commons Attribution 4.0 License (CC BY, <http://creativecommons.org/licenses/by/4.0/>), which permits unrestricted reuse of the work in any medium, provided the original work is properly cited. [DOI: 10.1149/1945-7111/ab9c87]



Manuscript submitted April 18, 2020; revised manuscript received June 6, 2020. Published June 29, 2020.

In many industrial sectors, stainless steels (SS) have a wide range of applications due to their high corrosion resistance in severe environments.¹ It is well known that this corrosion resistance originates from the surface oxide film covering the metallic substrate. Many studies have been carried out to characterize the composition and structure of the oxide film formed on SS surface in order to better understand the good corrosion resistance properties of the stainless steel.^{2–4} The performance of the oxide films (including the native and passive films) has been tested in various conditions, such as aqueous, gaseous and high temperature environments.^{5–7} Surface analysis, including X-ray Photoelectron Spectroscopy (XPS) and Time-of-Flight Secondary Ion Mass Spectrometry (ToF-SIMS), have demonstrated that the native oxide film formed on Fe-Cr based stainless steels generally shows a duplex structure, with an iron rich outer layer and a chromium rich inner layer.^{8–12} The chromium rich oxide plays a key role in the corrosion resistance.^{13,14} The passive film, formed electrochemically within the passive range in sulfuric acid, shows strong chromium enrichment compared to the native oxide film. This is attributed to the lower dissolution rate of chromium oxide compared to iron oxide in acidic media.^{8,11}

The knowledge of ion transport processes in the nanometer thick oxide layer is of major interest in order to better understand the nature, composition and thickness of the oxide film, and a prerequisite to control and optimize the functional properties of the stainless steels under varying operating conditions, such as electrolyzers, or gas sensors.^{15,16} A Cr_2O_3 scale is frequently used as a barrier to protect metallic alloys at high temperatures.¹⁷ As a consequence, the transport properties in Cr_2O_3 are of considerable interest.^{18–21} Poulain et al.²² investigated the oxide growth kinetics of Cr_2O_3 on a pure Cr substrate at 300 °C and under low oxygen pressure. Following a two step oxidation procedure starting with oxidation in $^{16}\text{O}_2$ gas and followed with a re-oxidation in $^{18}\text{O}_2$ isotopic tracer, they identified that the growth was controlled by anion transport via oxygen vacancies through the Cr_2O_3 layer. Following the same re-oxidation procedure, Voyshnis et al.²³ studied the oxidation behaviour of nickel-base alloy in high temperature water and in low O_2 gas pressure. They also showed that the process governing the oxide film growth is the inward (from the surface towards the metal/oxide interface) diffusion of oxygen species. Moreover, they showed an evolution of the inner oxide composition from Cr_2O_3 towards NiCr_2O_4 with increasing oxidation time. Recently, the two step oxidation procedure has also been used

with success to study the ion transport process governing the growth in a pre-formed passive film formed on 304 L SS in H_2SO_4 solution.²⁴ It was shown that during the low O_2 pressure re-oxidation step (exposure of the pre-formed film to the $^{18}\text{O}_2$ isotopic tracer), the outward diffusion of metallic cations governs the oxide growth.

Usually alloys containing small amounts of molybdenum, like 316 L SS, exhibit an improved resistance to the localized corrosion (pitting) in Cl-containing solutions. However, up to now, the effect of molybdenum addition on the ion-transport processes taking place during the growth of the oxide film is not well documented. Yu et al.²⁵ investigated the early stage oxidation of Ni-Cr and Ni-Cr-Mo alloys by using in situ transmission electron microscopy, and the effect of Mo was discussed. Based on their results, Mo doping in the alloy can both stabilize the cation vacancies and inhibit the voids formation in the oxide. Recently, Henderson et al.²⁶ studied by in situ ToF-SIMS the ion transport processes in Hastelloy BC-1 (Ni-Cr-Mo alloy) during re-oxidation under low O_2 pressure. The governing transport species were metallic cations, and the Mo rich outer layer seemed to be a barrier preventing the continued transport of Cr to the outermost layer.

The aim of the present work was to investigate by ToF-SIMS the ion transport processes in the native oxide and the passive film on 316 L SS during a re-oxidation step performed at 300 °C in low oxygen atmosphere. The passive film on 316 L SS was electrochemically formed at 0.4 V SCE⁻¹ in 0.05M H_2SO_4 solution for 1 h. The re-oxidation experiments were performed in situ by ToF-SIMS with ^{18}O isotopic marker to characterise the difference of ion transport processes in native and passive oxide films, and the effect of Mo on the ion transport.

Experimental

Sample preparation.—The 316 L SS was a Fe-19Cr-13Ni-2.7Mo (wt%) polycrystalline alloy. The sample surface was mechanically polished down to 0.25 μm with diamond paste and then successively washed with acetone, ethanol and water in ultrasonic bath for 10 min. The sample was then dried in compressed air. The native oxide film was formed by leaving the sample in air during 12 h. The passive film was formed electrochemically in 0.05M H_2SO_4 at 0.4 V SCE⁻¹ for 1 h.²⁷ After electrochemical passivation, the sample with passive film was taken out from the cell, rinsed with water, and then dried in compressed air.

A Gamry electrochemical workstation was used for electrochemical experiments. The electrochemical passivation was performed with a standard three-electrode cell with an Au counter electrode and a saturated calomel electrode as the reference electrode. The

*Electrochemical Society Fellow.

^zE-mail: philippe.marcus@chimieparitech.psl.fr

electrolyte was prepared with ultrapure chemicals (VWR[®]) and Millipore[®] water. Before measurement, the solution was deaerated by Ar bubbling for 30 min.

ToF-SIMS investigation.—ToF-SIMS depth profiles were obtained using a ToF-SIMS 5 spectrometer (IONTOF GmbH—Germany). A pulsed 25 keV Bi⁺ primary ion source was employed for analysis, delivering 1.2 pA current over a 100 × 100 μm² area. Depth profiling was carried out by interlacing secondary ion analysis with sputtering using a 0.5 keV Cs⁺ sputter beam giving a 17 nA target current over a 300 × 300 μm² area. Both Bi⁺ and Cs⁺ ion beams impinged the sample surface at an angle of 45° and were aligned in such a way that the analyzed ions were taken from the center of the sputtered crater.

ToF-SIMS depth profiles were used to determine the composition, structure and thickness of the oxide films (air-formed native oxide and passive oxide). The characteristic ions were selected as shown in Table I. The iron oxide in the native or passive films is associated with two different characteristic ions (⁵⁶Fe¹⁶O₂⁻ with high intensity and ⁵⁶Fe₂¹⁶O₃⁻ with a lower intensity). Since, in mass spectrometry, the characteristic ion of newly formed chromium oxide (⁵²Cr¹⁸O₂⁻) will overlap with the characteristic ion of pre-formed iron oxide (⁵⁶Fe¹⁶O₂⁻), ⁵²Cr¹⁸O₃⁻ and ⁵⁶Fe₂¹⁶O₃⁻ ions were used to characterize the oxide composition during re-oxidation in ¹⁸O₂ of the oxide pre-formed in H₂SO₄. It should be noted that the selected ions do not reveal the real stoichiometry of the species constituting the sample, but are the appropriate markers of the studied species. Since ToF-SIMS is a non-quantitative technique (due to a strong matrix effect on ion emission), the intensity of the plotted ions in the depth profiles cannot be compared directly and do not reflect the concentrations of the associated species in the substrate. However, ToF-SIMS depth profiles can be used to evaluate the intensity evolution for a given ion at different oxidation stages if the matrix remains similar. Thus, when a comparison between two samples is done for a similar matrix, it is considered that the ionization yield is similar for the two samples. In this study, we assume that despite the different passivation and/or heat treatments given to the 316 L SS substrates, the ionization yields of the oxidized species remain similar, making the comparison of the intensities of same ions between recorded ToF-SIMS depth profiles possible to evaluate the composition variation as function of the received treatment. The depth profiles are plotted vs the sputtering time. The sputtering rate has been calculated knowing for passivated 316 L SS (in H₂SO₄ at 0.4 V SCE⁻¹) (i) the total oxide layer thickness measured from XPS (results not shown here), and (ii) the position of the metal/oxide interface on the ToF-SIMS depth profile. Assuming a constant sputtering rate (0.02 nm s⁻¹) in the oxide, independent of the oxide layer composition, the sputtering time directly translates into oxide thickness.

Immediately after introduction of the specimen into the chamber, and prior to the application of heat, the air formed oxide was depth profiled using ToF-SIMS. Due to the destructive nature of sputtering, each depth profile was collected at a different, unperturbed area of the sample surface. The specimen was then heated up to a temperature of 300 ± 1 °C using the heating stage integrated in the

system. Modifications to the air-formed oxide due to temperature increase were analysed on both native and passive oxide films. After reaching 300 °C, a precision leak valve was then used to introduce ¹⁸O₂ into the analysis chamber, and the partial pressure P(¹⁸O₂) was maintained constant at 1 × 10⁻⁵ mPa. After a designated oxidation time, the gas inlet valve was closed while the sample temperature was maintained at 300 ± 1 °C, and the chamber immediately pumped down to the base pressure (10⁻⁹ mPa). A ToF-SIMS depth profile was then acquired in order to assess the oxide film growth mechanism.

Results and Discussion

Figure 1 shows the ToF-SIMS negative ion depth profiles for the (a) air-formed native oxide film and (b) the passive film formed at 0.4 V SCE⁻¹ in 0.05M sulfuric acid for 1 h, on 316 L SS surfaces. The secondary ions, selected for the interpretation of depth profiles, include ⁵²Cr¹⁶O₂⁻, ⁵⁶Fe¹⁶O₂⁻, ⁹⁸Mo¹⁶O₃⁻, ⁵⁶Fe₂⁻ and Ni₂⁻. The ions (⁵²Cr¹⁶O₂⁻, ⁵⁶Fe¹⁶O₂⁻, ⁹⁸Mo¹⁶O₂⁻) are used to characterize the corresponding oxides, while the ions (⁵⁶Fe₂⁻ and ⁵⁸Ni₂⁻) represent the underlying metallic substrate.^{24,26} The intensities of ⁵²Cr₂⁻ and Mo₂⁻ ions are extremely low (in negative ion polarity) and are not shown in the figure. As in previous papers, the maximum intensity of ⁵⁸Ni₂⁻ ion signal is used to define the oxide/metal interface.^{23,24,28} The thicknesses of the native and passive oxide films, corresponding to around ~80 s and 104 s of sputtering time, are 1.6 ± 0.2 nm and 2 ± 0.2 nm, respectively.

For the native oxide film, as shown in Fig. 1a, both the ⁵⁶Fe¹⁶O₂⁻ and ⁹⁸Mo¹⁶O₃⁻ depth profiles have their maximum in the outer part of the oxide film region, showing that oxidized iron and molybdenum are preferentially located in the outer region of the film. The ⁵²Cr¹⁶O₂⁻ depth profile shows its peak in the inner part of the oxide film, indicating that chromium oxide is concentrated in the inner oxide layer. For the passive film (Fig. 1b), while the ⁹⁸Mo¹⁶O₃⁻ depth profile exhibits a similar trend (maximum intensity in the outer oxide) as the one observed for the native oxide, indicating that oxidized molybdenum is located in the outer film, the ⁵⁶Fe¹⁶O₂⁻ depth profile is slightly different. ⁵⁶Fe¹⁶O₂⁻ maximum intensity is still located in the outer oxide (with a lower intensity compared to that measured on the native oxide), but decreases slowly though the inner oxide film. This indicates that iron oxide is still mainly located in the outer film, but is also present in the inner oxide film. Finally, the ⁵²Cr¹⁶O₂⁻ depth profile has its maximum in the inner oxide region but displays a wider peak width compared to that of the native oxide layer. This indicates a thicker, Cr rich, inner oxide film, which contributes to a thickening of the passive film.

Both the native and passive films have duplex structures, with a Mo and Fe rich outer layer and a Cr rich inner layer (possibly including more Fe oxide in the inner layer of the passive film). Passivation by anodic polarization increased the oxide film thickness, which corresponds to the thickening of the Cr rich inner layer. The concentration of iron oxide in the outer film is reduced after passivation, which is due to the enhanced dissolution of iron oxide in sulfuric acid.⁸

Table I. ToF-SIMS characteristic ions used to investigate the composition and structure of the oxide films formed on 316 L SS.

	Species	Characteristic ion
Metallic substrate	Metallic Fe	⁵⁶ Fe ₂ ⁻
	Metallic Ni	⁵⁸ Ni ₂ ⁻
Pre-formed oxide (¹⁶ O)	Iron oxide	⁵⁶ Fe ¹⁶ O ₂ ⁻ ; ⁵⁶ Fe ₂ ¹⁶ O ₃ ⁻
	Chromium oxide	⁵² Cr ¹⁶ O ₂ ⁻
	Molybdenum oxide	⁹⁸ Mo ¹⁶ O ₃ ⁻
	Iron oxide	⁵⁶ Fe ¹⁸ O ₂ ⁻
Newly-formed oxide (¹⁸ O)	Iron oxide	⁵⁶ Fe ¹⁸ O ₂ ⁻
	Chromium oxide	⁵² Cr ¹⁸ O ₃ ⁻
	Molybdenum oxide	⁹⁸ Mo ¹⁸ O ₃ ⁻

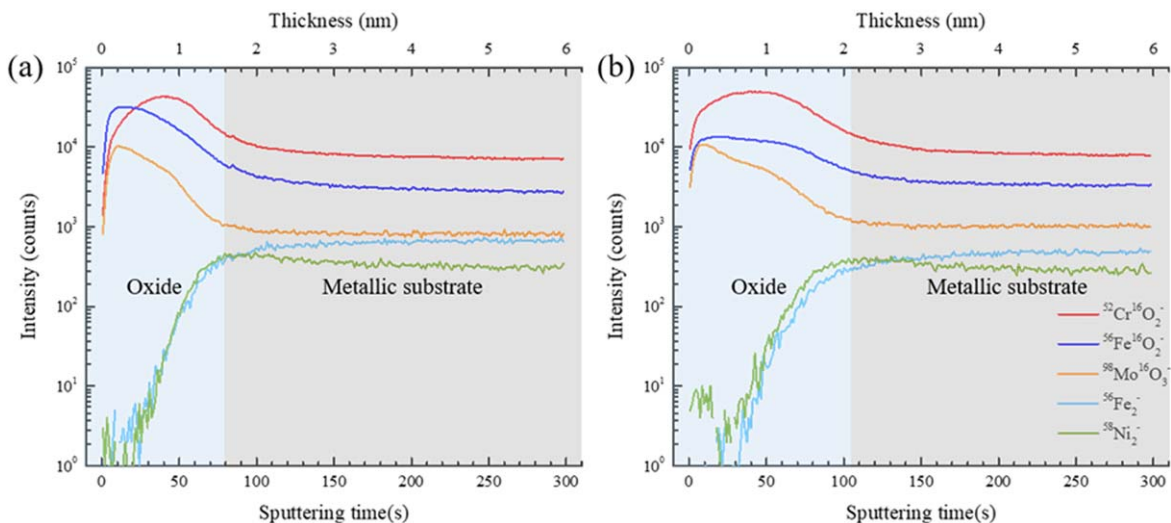


Figure 1. ToF-SIMS depth profiles of (a) the air-formed native oxide film and (b) the passive oxide film formed on 316 L SS at room temperature (The passive film was formed electrochemically on 316 L SS surface in 0.05M $\text{H}_2\text{SO}_4(\text{aq})$ at 0.4 V SCE^{-1} for 1 h).

The in situ re-oxidation experiments in the ToF SIMS were carried out at $300 \text{ }^\circ\text{C}$. Such experiments have been already described in a previous study.^{24,27} The thermal stability of both the native and passive films have been studied. Figure 2 shows the depth profiles of the native and passive films recorded immediately after heating up to $300 \text{ }^\circ\text{C}$ under high vacuum conditions in the ToF-SIMS chamber. Based on the maximum intensities of Ni_2^- depth profiles, the oxide/metal interface for native and passive films are located at 80 s and 92 s of sputtering time, corresponding to oxide thicknesses of $1.6 \pm 0.2 \text{ nm}$ and $1.8 \pm 0.2 \text{ nm}$, respectively. The native oxide film thickness remains unchanged at $300 \text{ }^\circ\text{C}$, while the passive film thickness decreases.

For the native oxide film (Fig. 2a), the $^{98}\text{Mo}^{16}\text{O}_3^-$ and $^{56}\text{Fe}^{16}\text{O}_2^-$ depth profiles still peak in the outer oxide film, and the $^{52}\text{Cr}^{16}\text{O}_2^-$ depth profile has its maximum in the inner film. Thus, Mo and Fe oxides are preferentially located in the outer layer, and Cr oxide is rich in the inner layer. It is noticed that the width of $^{56}\text{Fe}^{16}\text{O}_2^-$ depth profile is now narrower, while the width of $^{52}\text{Cr}^{16}\text{O}_2^-$ depth profile is wider compared to the native film at room temperature, showing the thickening of the chromium rich inner layer at the expense of the iron rich outer layer.²⁴ Looking at the $^{98}\text{Mo}^{16}\text{O}_3^-$ signal, it also shows a narrower width in the outer oxide layer, meaning that molybdenum is more concentrated in this outer oxide layer.

After heating the passive film at $300 \text{ }^\circ\text{C}$ in vacuum the Mo content in the outer oxide layer is higher (Fig. 2b). Whereas the $^{98}\text{Mo}^{16}\text{O}_3^-$ signal was almost distributed through the total layer thickness at room temperature (with a higher content in the outer oxide), it is, at $300 \text{ }^\circ\text{C}$, mainly localized in the outer oxide. Moreover, heating the sample up to $300 \text{ }^\circ\text{C}$ also has an effect on the $^{52}\text{Cr}^{16}\text{O}_2^-$ signal profile that becomes wider and on the $^{56}\text{Fe}^{16}\text{O}_2^-$ signal profile that becomes narrower and exhibits a lower intensity in the outer oxide layer (up to 50 s of sputtering approximately). Those modifications are attributed to formation of Cr oxide at the expense of the Fe oxide, partial decomposition of hydroxide and removal of water ligands as already observed on passivated 304 L SS when exposed to high temperature.^{24,27} Thus, the decrease of the passive oxide film thickness is attributed to the dehydroxylation and dehydration. For the native oxide film, reduction of iron oxide and formation of chromium oxide are mainly observed. The enhanced dehydroxylation and dehydration of the passive film is not surprising, since after passivation the hydroxide and the water ligand contents in the film are high.

Figure 3 shows the ToF-SIMS negative ion depth profiles obtained on the native oxide film on 316 L SS surface after exposure to isotopic $^{18}\text{O}_2$ gas (10^{-5} mbar) at $300 \text{ }^\circ\text{C}$ for different times. After 1 min of re-oxidation (Fig. 3a), the metal/oxide interface, always

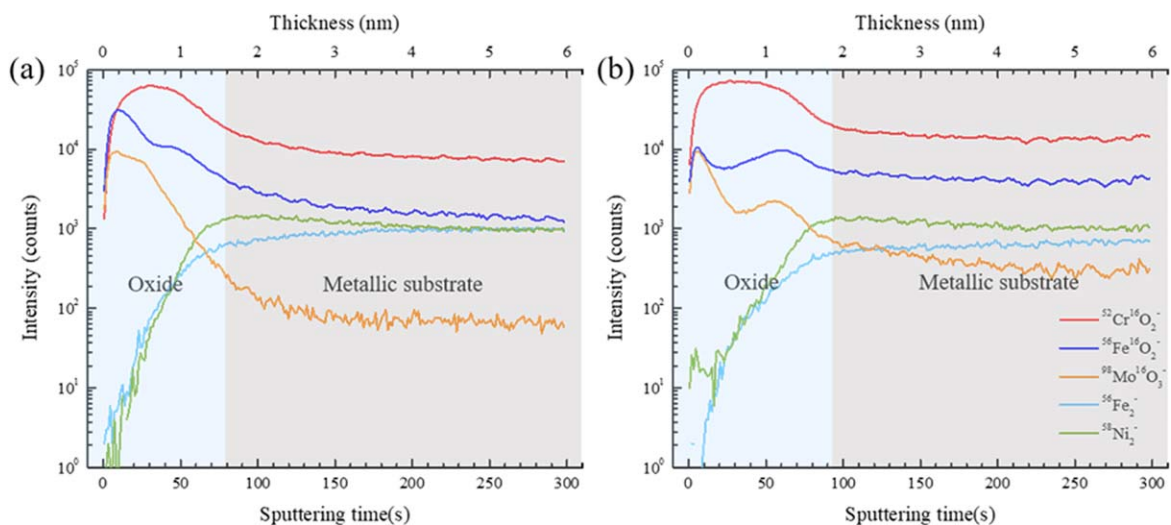


Figure 2. ToF-SIMS depth profiles of (a) the native oxide and (b) the passive film on 316 L SS at $300 \text{ }^\circ\text{C}$.

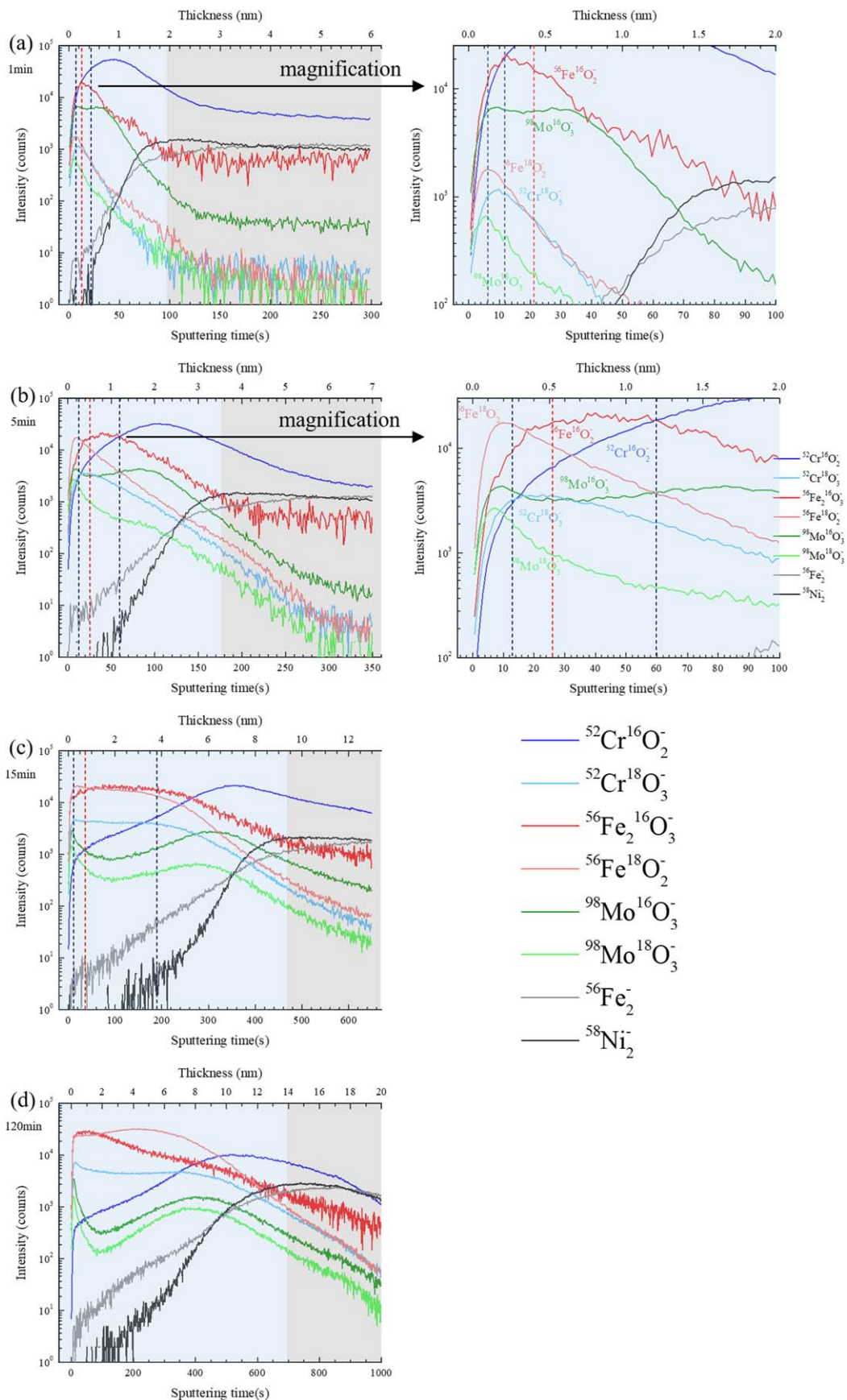


Figure 3. ToF-SIMS profiles obtained on the native oxide film formed on 316 L SS surface after re-oxidation at 300 °C for (a) 1 min, (b) 5 min, (c) 15 min and (d) 2 h. (The intensity of $^{56}\text{Fe}_2^{16}\text{O}_3^-$ signal is multiplied by 50).

defined by the maximum intensity of the Ni_2^- signal, is located at 100 s of sputtering time, corresponding to a thickness of 2 nm. Looking at the characteristic ions ($^{52}\text{Cr}^{18}\text{O}_3^-$, $^{56}\text{Fe}^{18}\text{O}_2^-$ and $^{98}\text{Mo}^{18}\text{O}_3^-$) of the newly formed oxide (^{18}O) species, the maximum intensity locations of these depth profiles are in the outermost region of the film, demonstrating that the newly formed oxides are concentrated at the outer surface of the native film. Thus, the governing ion transport mechanism in the native oxide film on 316 L SS is cation diffusion.

After exposure to $^{18}\text{O}_2$ for 5 min (Fig. 3b), the oxide film thickens from 2 ± 0.2 nm to 3.6 ± 0.2 nm (corresponding to 178 s of sputtering). The locations of maximum intensities of the new oxide (^{18}O) species are again found in the outer layer (ranging from 0 s to 60 s of sputtering), while the inner layer (ranging from 60 s to 178 s of sputtering) remains the previously formed Cr oxide (^{16}O). A closer look at the distributions of each species ($^{52}\text{Cr}^{18}\text{O}_3^-$, $^{56}\text{Fe}^{18}\text{O}_2^-$, $^{98}\text{Mo}^{18}\text{O}_3^-$, $^{98}\text{Mo}^{16}\text{O}_3^-$ and $^{56}\text{Fe}_2^{16}\text{O}_3^-$) in the outer oxide layer, corresponding to the region from 0 s to 60 s of sputtering time, shows that this region can be divided into three parts. The first part, representing the outermost layer (0 s to 13 s of sputtering time), is comprised of the newly formed Mo, Fe oxides (^{18}O), and the original Mo oxide (^{16}O). The middle region (13 s to 26 s of sputtering time) is rich in the newly formed Cr oxide (^{18}O). The third part (26 s to 60 s of sputtering time) is the original Fe rich oxide (^{16}O) layer. Thus, the Mo-rich outermost oxides (^{16}O and ^{18}O) layer appears to play the role of a barrier layer for the continued diffusion of chromium cations toward the oxygen gas/oxide interface, while this Mo-rich layer does not prevent the diffusion of Fe cations to the oxide surface. Thus, the formation of the new chromium oxide (^{18}O) needs the ^{18}O ions penetration through the Mo-rich outer oxide (^{16}O and ^{18}O) layer to react with Cr cations diffusing from the substrate. This interpretation is supported by the clear evidence that the Mo-free oxides have Cr oxide (^{18}O) in the outer oxide.²⁴

When the re-oxidation time reaches 15 min (Fig. 3c), the oxide film thickness is 9.4 ± 0.2 nm (470 s of sputtering time). The intensities from ^{18}O -containing ions markedly increased, especially the intensity of $^{56}\text{Fe}^{18}\text{O}_2^-$ ion, which is approximately equal to that of $^{56}\text{Fe}_2^{16}\text{O}_3^-$ ion, the characteristic ion of the pre-formed Fe oxide (^{16}O). The fast increasing of Fe 18-oxide signal ($^{56}\text{Fe}^{18}\text{O}_2^-$) in the oxide compared to that of Cr oxide (^{18}O) ($^{52}\text{Cr}^{18}\text{O}_3^-$), is a consequence of the blocking effect of the Mo rich oxide layer on diffusion of Cr ions. The effect of isotopic exchange between ^{18}O and ^{16}O , which was already reported and discussed in previous studies,²²⁻²⁴ cannot be ignored. It causes peak broadening for all oxidized species with increasing re-oxidation time.

After a re-oxidation time of 120 min (Fig. 3d), the oxide film thickness is around 14 nm (700 s of sputtering time). The $^{56}\text{Fe}^{18}\text{O}_2^-$ signal has shifted its maximum intensity from the external surface before 15 min of re-oxidation to the internal oxide, which is assigned mainly to isotopic exchange between ^{18}O with ^{16}O species.

The re-oxidation study was also performed for the passive film on 316 L SS, and the results are shown in Fig. 4. Using the same data analysis method, we can conclude that the ion-transport mechanisms in the passive film on 316 L SS are the same as in the native oxide film. Cation diffusion is the governing process for oxide film growth. The molybdenum rich outer oxide layer is a barrier for the diffusion of Cr towards the outermost oxide surface. During oxidation, isotopic exchange between the ^{18}O and ^{16}O species is observed.

A schematic depiction of the ion transport process for the oxide films (native and passive) formed on 316 L SS is shown in Fig. 5. At the early re-oxidation stage, the governing ion transport mechanism in oxide film is the outward cations diffusion, meaning the metallic ions (Mo, Fe and Cr) diffuse from the metallic substrate towards the outer surface. Meanwhile, the Mo rich outermost layer acts as a barrier that blocks the further diffusion of Cr to the oxygen gas/oxide interface. Thus, the governing step also includes the penetration of oxygen through the Mo rich oxide layer. The newly formed Mo and Fe oxides are located in the outer layer, while the newly formed Cr

oxide is under this outermost layer. For long exposure to oxygen, isotopic exchange between the ^{18}O and ^{16}O species dominates. Some volatilization of chromium oxide, evidenced by Poulain et al.²² for oxidation of pure Cr at the same temperature, cannot be excluded.

Since the thickness of the oxide layer can be measured based on the ToF-SIMS profiles obtained for different oxidation times, we can determine the growth rate of the oxide at 300 °C. The data are shown in Fig. 6, and the data previously reported for the passive film on 304 L SS are shown for comparison.²⁴

The kinetics of oxidation seems to follow a logarithmic-type law, which, according to previous work, can be explained by the competition between parabolic growth and oxide layer volatilization.^{22,24} Although volatilization is a well-known phenomenon at very high temperature, it has been shown by Poulain et al.²² that volatilization of oxide and particularly Cr oxide also happens at lower temperature. Thus, oxide volatilization must be taken into account to explain the kinetics of oxide film growth on stainless alloys even at medium temperature. From Fig. 6, two parts can be observed on each curve. In the first part (before about 1 h of re-oxidation) the oxide layer grows rapidly (newly formed outer oxide layer). Then, after 1 h of re-oxidation, the growth of the oxide layer is slow, and a quasi-stationary film thickness is observed (growth rate about equal to volatilization rate).

We can notice that the oxide growth on the passive film of 316 L SS at 300 °C is significantly slower than on the native oxide film (Fig. 6). The passive film thickness after 120 min re-oxidation in $^{18}\text{O}_2$ is 6 nm, which is much lower than that of the native oxide film (14 nm). The different oxidation rates between native and passive oxide films can be attributed to the different composition and structure of the films. Firstly, the passive film has higher Cr content and less Fe compared to the native oxide film, as already evidenced by previous XPS results obtained on 316 L SS.^{8,11} The ion diffusion coefficient in chromium oxide is known to be much lower than that in iron oxide, due to a lower concentration of ionic defects in chromium oxide.²⁹⁻³³ Moreover, passive films are known to have less grain boundaries, which are fast diffusion paths for the diffusing species, than air-formed native oxide, due to the coalescence of the oxide grains induced by electrochemical passivation, as shown previously.^{11,34,35} This was shown to result in larger lateral grain dimensions for passive film than air-formed native oxide on 316 L SS surface (11.5 ± 2.6 nm and 5.3 ± 0.9 nm, respectively). Thus, passive films with larger grain size have less grain boundary than native oxide films, making the oxidation rate of passive oxide films lower than that of native oxide films.

When we look at the oxidation kinetics on passive films on 304 L SS and 316 L SS, we observe a lower oxidation rate for the 316 L SS, which can be assigned to the Mo-rich outer oxide layer, which acts as a barrier preventing Cr diffusion to the outer surface. The growth of the chromium-rich oxide film requires both the diffusion of Cr from the substrate and the penetration of oxygen through the Mo-rich outer oxide layer.

The oxidation kinetics can then be fitted by Eq. 1, as shown in the previous papers.²²⁻²⁴

$$t = \frac{k_p}{k_v^2} \left[-\frac{k_v}{k_p} (x - x_0) - \ln \left(1 - \frac{k_v}{k_p} (x - x_0) \right) \right] \quad [1]$$

where k_p is the parabolic constant, k_v is the constant of volatilization, and x_0 is the thickness of pre-formed oxide film.

The fittings of the curves are also shown in Fig. 6, and the results calculated for the parabolic and volatilization constants are given in Table II.

From Table II we can see that, for the native film on 316 L SS, the value of k_p derived from the fit is $7.9 \times 10^{-2} \text{ nm}^2 \cdot \text{s}^{-1}$ and k_v is $6 \times 10^{-3} \text{ nm} \cdot \text{s}^{-1}$. These values are markedly higher than that calculated for passive films on 316 L SS ($k_p = 3 \times 10^{-3} \text{ nm}^2 \cdot \text{s}^{-1}$ and $k_v = 4 \times 10^{-4} \text{ nm} \cdot \text{s}^{-1}$) and 304 L SS ($k_p = 1.8 \times 10^{-2} \text{ nm}^2 \cdot \text{s}^{-1}$ and $k_v = 4 \times 10^{-3} \text{ nm} \cdot \text{s}^{-1}$). This is mainly due to the fact that the

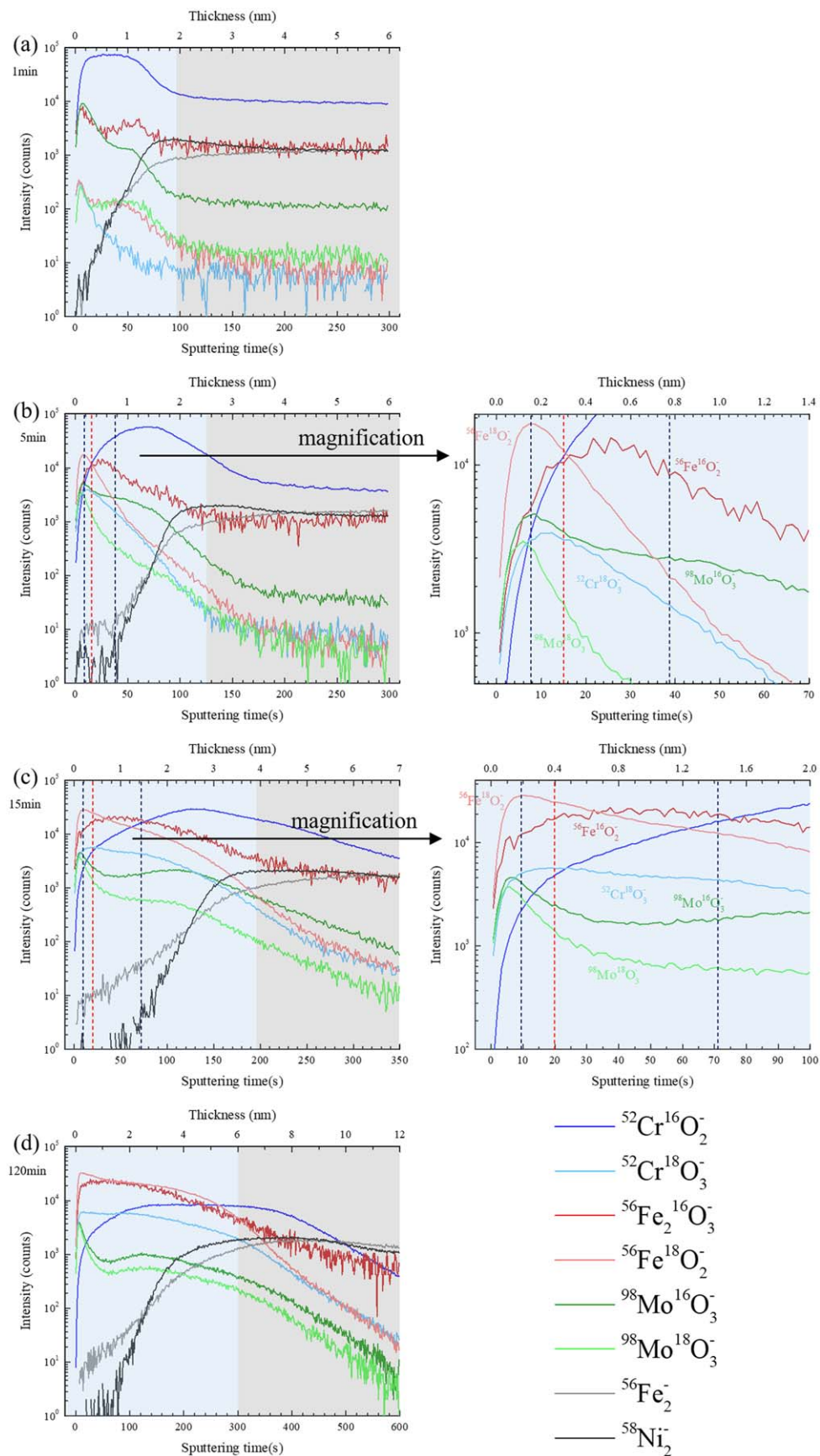


Figure 4. ToF-SIMS profiles obtained on the passive film formed on 316 L SS surface after re-oxidation at 300 °C for (a) 1 min, (b) 5 min, (c) 15 min and (d) 2 h. (The intensity of $^{56}\text{Fe}_2^{16}\text{O}_3^-$ signal is multiplied by 70).

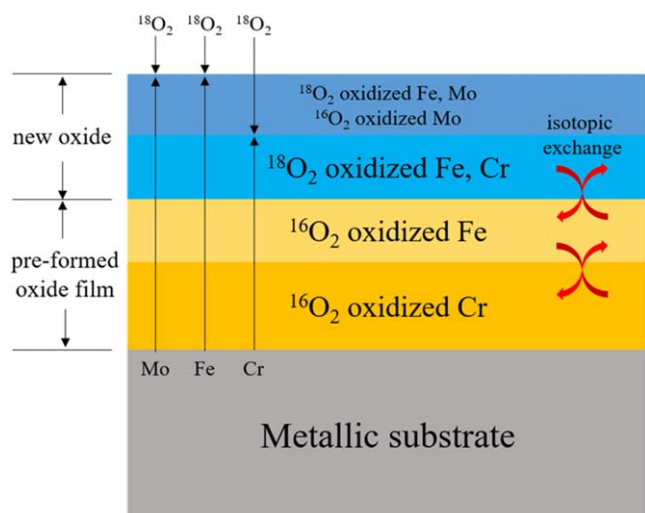


Figure 5. Scheme of the ion transport mechanisms for oxide films (native oxide and passive film) formed on 316 L stainless steel.

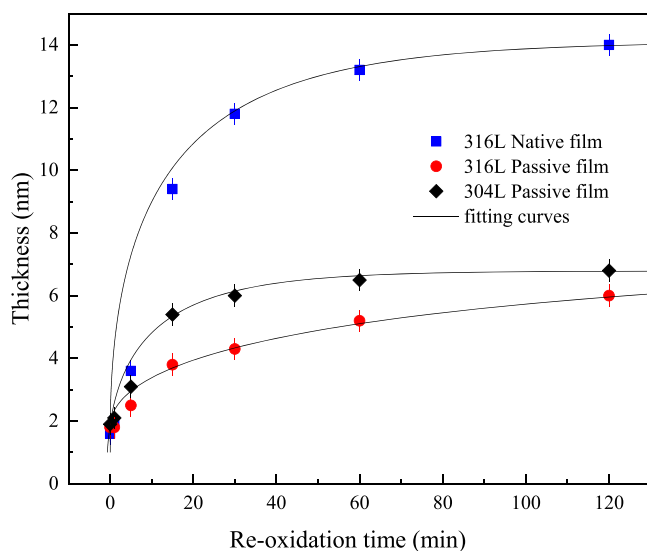


Figure 6. Re-oxidation kinetics (experimental data and fit) for the native and passive films on 316 L SS, and passive film on 304 L SS (from Ref. 24) at 300 °C ($^{18}\text{O}_2$ pressure = 10^{-5} mbar).

Table II. Oxidation kinetics of the native and passive films on 316 L SS, and passive film on 304 L SS at 300 °C.

	k_p ($\text{nm}^2 \cdot \text{s}^{-1}$)	k_v ($\text{nm} \cdot \text{s}^{-1}$)
316 L SS Native oxide	0.079	0.006
316 L SS Passive film	0.003	0.0004
304 L SS Passive film	0.018	0.004

native oxide film has: (i) a higher grain boundary density that react as fast diffusion path for the diffusing species, and (ii) a lower Cr oxide content compared to the electrochemically formed passive film. When we compared the k_p and k_v values for the passive films on 316 L SS and 304 L SS, the values for 316 L SS are almost one magnitude lower than that for 304 L SS. This is attributed to the Mo outer most layer, which inhibits the diffusion of Cr and also prevents the exposure of Cr oxide in the outer surface.

Assuming that only the outward cation diffusion is the governing ion transport for oxide growth (an oversimplified view as oxygen

diffusion through the outer Mo layer has been shown to be required), and using a simplified relationship between diffusion coefficient and parabolic rate constant $k_p = 2D_c$,^{24,36} the outward cation diffusion coefficient (D_c) in the oxide film is $1.5 \times 10^{-17} \text{ cm}^2 \cdot \text{s}^{-1}$ and $4 \times 10^{-16} \text{ cm}^2 \cdot \text{s}^{-1}$ for passive film and native film, respectively. The chromium content and possibly the grain size in the passive film have significantly decreased the cation diffusion coefficient in the film.

Conclusions

The transport of ions in oxide films (both the native and passive films) on 316 L SS surfaces has been investigated by ToF-SIMS with ^{18}O isotopic tracer. The native oxide film was formed in air, whereas the passive oxide film was formed electrochemically in 0.05M sulfuric acid at 0.4 V SCE^{-1} for 1 h. Both the native film and passive film have duplex structures with a Mo and Fe rich outer layer and a Cr rich inner layer. Passivation in sulfuric acid causes oxide enrichment in Cr due to the preferential dissolution of the Fe oxide. The native oxide film is quasi stable in vacuum up to 300 °C, while the passive film becomes thinner at this temperature, due to dehydroxylation and dehydration of the oxide.

The results of in situ re-oxidation of the oxide films (native and passive films) on 316 L SS surface at 300 °C with ^{18}O isotopic tracer reveal that the governing ion transport is the outward diffusion of metallic cations (Cr, Fe and Mo) to the oxide surface. The outer Mo-rich oxide layer acts as a barrier preventing the further diffusion of Cr to the oxygen gas/oxide interface, while it has no barrier effect on the diffusion of Fe and Mo. Based on a model taking into account oxidation and possible volatilization, the measured oxide growth kinetics was fitted. The parabolic oxidation constant for the native oxide is $7.9 \times 10^{-2} \text{ nm}^2 \cdot \text{s}^{-1}$, while it is only $3 \times 10^{-3} \text{ nm}^2 \cdot \text{s}^{-1}$ for the passive film. The higher Cr content, and a lower density of grain boundary in the passive oxide, significantly reduce the re-oxidation rate of passive oxide film. A very significant role of the Mo rich outer oxide layer, acting as a barrier to Cr outward diffusion, is evidenced by the use of ^{18}O isotopic label.

Acknowledgments

This project has received funding from the European Research Council (ERC) under the European Union's Horizon 2020 research and innovation program (ERC Advanced grant CIMNAS: Corrosion Initiation Mechanisms at the Atomic and Nanometric Scales, grant no. 741123). Région île-de-France is acknowledged for partial funding of the ToF-SIMS equipment. China Scholarship Council (CSC) is acknowledged for the scholarship to the first author (No. 201706460018).

ORCID

Philippe Marcus  <https://orcid.org/0000-0002-9140-0047>

References

1. A. J. Sedriks, *Corrosion of Stainless Steel* (John Wiley & Sons, Inc, United States) 2nd ed. (1996).
2. V. Maurice and P. Marcus, *Prog. Mater. Sci.*, **95**, 132 (2018).
3. H.-H. Strehblow, *Electrochim. Acta*, **212**, 630 (2016).
4. Z. Feng, X. Cheng, C. Dong, L. Xu, and X. Li, *Corros. Sci.*, **52**, 3646 (2010).
5. V. Maurice and P. Marcus, *Electrochim. Acta*, **84**, 129 (2012).
6. C.-O. Olsson and D. Landolt, *Electrochim. Acta*, **48**, 1093 (2003).
7. S. R. J. Saunders, M. Monteiro, and F. Rizzo, *Prog. Mater. Sci.*, **53**, 775 (2008).
8. Z. Wang, F. Di-Franco, A. Seyeux, S. Zanna, V. Maurice, and P. Marcus, *J. Electrochem. Soc.*, **166**, C3376 (2019).
9. E. Gardin, S. Zanna, A. Seyeux, A. Allion-Maurer, and P. Marcus, *Corros. Sci.*, **155**, 121 (2019).
10. E. Gardin, S. Zanna, A. Seyeux, A. Allion-Maurer, and P. Marcus, *Corros. Sci.*, **143**, 403 (2018).
11. V. Maurice, H. Peng, L. H. Klein, A. Seyeux, S. Zanna, and P. Marcus, *Faraday Discuss.*, **180**, 151 (2015).
12. L. Ma, F. Wiame, V. Maurice, and P. Marcus, *Corros. Sci.*, **140**, 205 (2018).
13. Z. Wang, E.-M. Paschalidou, A. Seyeux, S. Zanna, V. Maurice, and P. Marcus, *Frontiers in Materials*, **6**, 232 (2019).
14. V. Maurice, W. Yang, and P. Marcus, *J. Electrochem. Soc.*, **141**, 3016 (1994).

15. A. Tuthill, *Nickel Development Institute (NiDI): Toronto, ON, Canada*, 47 (2002).
16. M. Palcut, L. Mikkelsen, K. Neufeld, M. Chen, R. Knibbe, and P. V. Hendriksen, *Corros. Sci.*, **52**, 3309 (2010).
17. A. M. Huntz and S. C. Tsai, *J. Mater. Sci. Lett.*, **13**, 821 (1994).
18. S. Tsai, A. Huntz, C. Dolin, and C. Monty, *Radiat. Eff. Defects Solids*, **137**, 285 (1995).
19. S. C. Tsai, A. M. Huntz, and C. Dolin, *Oxid. Met.*, **43**, 581 (1995).
20. S. C. Tsai, A. M. Huntz, and C. Dolin, *Mater. Sci. Eng. A*, **212**, 6 (1996).
21. A. Sabioni, A. Huntz, L. Borges, and F. Jomard, *Philos. Mag.*, **87**, 1921 (2007).
22. C. Poulain, A. Seyeux, S. Voyshnis, and P. Marcus, *Oxid. Met.*, **88**, 423 (2017).
23. S. Voyshnis, A. Seyeux, S. Zanna, B. Martin-Cabanas, T. Couvant, and P. Marcus, *Corros. Sci.*, **145**, 212 (2018).
24. L. Wang, S. Voyshnis, A. Seyeux, and P. Marcus, *Corros. Sci.*, **173**, 108779 (2020).
25. X.-x. Yu, A. Gulec, C. M. Andolina, E. J. Zeitchick, K. Gusieva, J. C. Yang, J. R. Scully, J. H. Perepezko, and L. D. Marks, *Corrosion*, **74**, 939 (2018).
26. J. D. Henderson, A. Seyeux, S. Zanna, M. C. Biesinger, D. W. Shoesmith, J. J. Noël, and P. Marcus, *Corros. Sci.*, **159**, 108138 (2019).
27. L. Wang, A. Seyeux, and P. Marcus, *Corros. Sci.*, **165**, 108395 (2019).
28. X. Wu, S. Voyshnis, A. Seyeux, Y. Chumlyakov, and P. Marcus, *Corros. Sci.*, **141**, 175 (2018).
29. G. Wallwork, *Rep. Prog. Phys.*, **39**, 401 (1976).
30. K. Hoshino and N. Peterson, *J. Am. Ceram. Soc.*, **66**, c202 (1983).
31. M. J. Graham, J. Eldrige, D. Mitchell, and R. Hussey, *Mater. Sci. Forum*, **43**, 207 (1989).
32. A. C. S. Sabioni, A. M. Huntz, J. Philibert, B. Lesage, and C. Monty, *J. Mater. Sci.*, **27**, 4782 (1992).
33. A. C. S. Sabioni, A. M. J. Daniel, W. Macedo, M. Martins, A. M. Huntz, F. Jomard, and A. Persiano, *Defect and Diffusion Forum*, **237**, 277 (2005).
34. V. Maurice, W. Yang, and P. Marcus, *J. Electrochem. Soc.*, **145**, 909 (1998).
35. V. Maurice, W. Yang, and P. Marcus, *J. Electrochem. Soc.*, **143**, 1182 (1996).
36. N. Perez, *Electrochemistry and Corrosion Science* (Springer, New York) (2004).